Materials Advances

ROYAL SOCIETY OF CHEMISTRY

PAPER

View Article Online
View Journal | View Issue

Cite this: *Mater. Adv.*, 2024, 5, 8836

Advanced morphological control over Cu nanowires through a design of experiments approach†

Andrea Conte, Antonella Rosati, Marco Fantin, Alessandro Aliprandi, Marco Baron, Sara Bonacchi and Sabrina Antonello *

Received 17th April 2024,
Accepted 29th September 2024

DOI: 10.1039/d4ma00402g

rsc.li/materials-advances

Copper nanowires (CuNWs), featuring anisotropic highly conductive crystalline facets, represent an ideal nanostructure to fabricate on-demand materials as transparent electrodes and efficient electrocatalysts. The development of reliable and robust CuNWs requires achieving a full control over their synthesis and morphology growth, a challenge that continues to puzzle materials scientists. In this study, we systematically investigated the correlation between the critical synthetic parameters and the structural properties of nanowires using a design of experiments (DOE) approach. Multiparametric variation of experimental reaction conditions combined with orthogonal technical analysis allowed us to develop a sound predictive model that provides guidelines for designing CuNWs with controlled morphology and reaction yield. Beyond these synthetic achievements, voltammetric and electrocatalytic experiments were used to correlate the CuNWs morphology and structure to their catalytic activity and selectivity toward CO_2 electroreduction, thus opening new avenues for further intersectoral actions.

1. Introduction

Since the emergence of nanotechnology, the miniaturization of materials to a scale where size-, shape-, surface-, and defect-dependent effects operate has opened ambitious challenges not only from a technological perspective but also from a visionary perspective. The innovative opportunity conferred to the elements of the periodic table within the nanostructured materials has highlighted plenty of unexpected distinct properties and functions.[1] In this framework, copper stands as one of the most pivotal elements that has been exploited to demonstrate the effect of size and structure modification in order to enhance its inherent bulk properties, such as its high electrical conductivity, towards a wider range of emerging applications.[2–11]

One-dimensional copper nanowires (CuNWs), featuring a high aspect ratio (AR > 100) due to their nanometer-size diameter and hundreds of micrometers length,[5,12] have been recently investigated to obtain insights into the strong correlations among composition, shape, and surface properties[13–16] for developing highly transparent conductive electrodes for application in electronic devices, such as touch screens[17] or solar cells,[18] as well as in flexible transistors[19] and biosensors.[20,21] More recently, enhanced electrocatalytic properties towards the production of renewable energy sources such as hydrogen and green carbon-based fuels[5,22] have been attributed to the sophisticated manipulations of different crystalline facets within the wires.[6,23] Since then, multidisciplinary methods, such as chemical reduction,[24,25] physical vapor deposition,[26] and electrochemical deposition,[27] have been engineered for the synthesis of tailored CuNWs. In particular, the hydrothermal approach, which is based on the reduction of a Cu(II)–complex in aqueous solutions in the presence of surfactants at room temperature,[6,28] stands out for its cost, mild conditions, environmental impact, and promising scalability. Despite significant improvements, the ultimate control over the CuNWs morphology and crystallinity has not been achieved yet, suggesting the need for a more comprehensive investigation of the interconnected synthetic parameters, such as copper source, temperature, reaction time, and pH as well as, the type and amount of surfactant and reducing agent to ultimately regulate the final outcome and performances.[6,23,29–35]

The design of experiments (DOE) method is a well-established method to study the relationship between multiple input variables and key output variables.[36,37] In recent years, DOE has attracted much attention from the community of nanomaterials scientists and engineers to progress in the elucidation of the synthetic parameters governing the size and structure of nanoparticles.[37–43] This method enables the formulation of predictive models with limited experimental effort and

Department of Chemical Sciences, University of Padova, Via F. Marzolo 1, 35131, Padova, Italy. E-mail: sabrina.antonello@unipd.it

† Electronic supplementary information (ESI) available. See DOI: https://doi.org/10.1039/d4ma00402g

facilitates the detection of interactions between different experimental conditions, which would be challenging to recognize using a one-factor-at-a-time approach. The current main challenge in data-driven material optimization arises from the scarcity and quality of input data.[44] In situations where comparable data are lacking, DOE sampling techniques can be invaluable in generating datasets well-suited for modeling.[45] Here, we demonstrate how both morphological structures, such as the thickness and aspect ratio, and the reaction yield of CuNWs can be controlled and rationalized by enrolling only four simple parameters in hydrothermal synthesis such as the reaction time, temperature, and type and concentration of reducing agent within a multivariate DOE approach. In particular, we implement the utility of DOE to extract the maximum information from straightforward experiments and to yield statistically robust results while minimizing the synthetic efforts in terms of time and materials. Beyond these synthetic achievements, we also lay the foundation for a complete understanding of the pivotal role played by the CuNWs' morphologies and regulated features towards highly selective electrocatalyst materials for CO_2 reduction.

2. Results and discussion

CuNWs were synthesized according to a hydrothermal method, as previously reported[30] with some modifications detailed in the Experimental section. In particular, $CuCl_2{\cdot}2H_2O$ was used as the copper source and 1-octadecylamine (ODA) (4 equivalents) was used as the capping agent in all the performed syntheses. As reported,[23,31,46] the presence of ODA guarantees the anisotropic growth of the Cu seed crystals by selectively bonding to the (100) facet and leaving the (111) facet free. This configuration results in a five-fold twinned structure with five (100) side surfaces along the [110] direction. Alkylamines with chains longer than sixteen carbon atoms are needed to obtain CuNWs of good quality.[6,47] Besides guaranteeing the anisotropic growth of the CuNWs, the use of alkylamines is instrumental in protecting their surface from oxidation. Indeed, CuNWs synthesized under these conditions are stable for months when dispersed in ethanol solution, in contrast to CuNWs synthesized without capping agents.[48] Here, we explore the variables, reaction time, temperature, and type and concentration of the reducing agent to map the chemical reaction space. In particular, we selected glucose and sodium ascorbate as reducing agents because they are environmentally friendly, non-toxic and low-cost reagents. Fig. 1 outlines our workflow for investigating how CuNWs' yield and morphology are influenced by synthetic parameters. The framework mirrors classical DOE procedures, starting with a screening design phase to identify key parameters impacting CuNWs' characteristics. Subsequently, our approach utilized "definitive screening design" (DSD) to delve deeper into selected variables, elucidating their relationships and directing their effects toward achieving the desired CuNW morphology. Quantitative measurements of the CuNW structure included the diameter (obtained from SEM images) and the parameter Ψ, defined as the ratio of the maximum intensity of two XRD signals (111)/(200) in the diffractogram, which is known to be correlated with the aspect ratio of CuNWs.[49] Additionally, the yield of the reactions was analyzed as a screening output of the synthesis conditions. SAS JMP Pro software was used to perform the experimental design, randomize the order of the experiments, evaluate the model, and obtain the effects of each reaction parameter and their interactions.

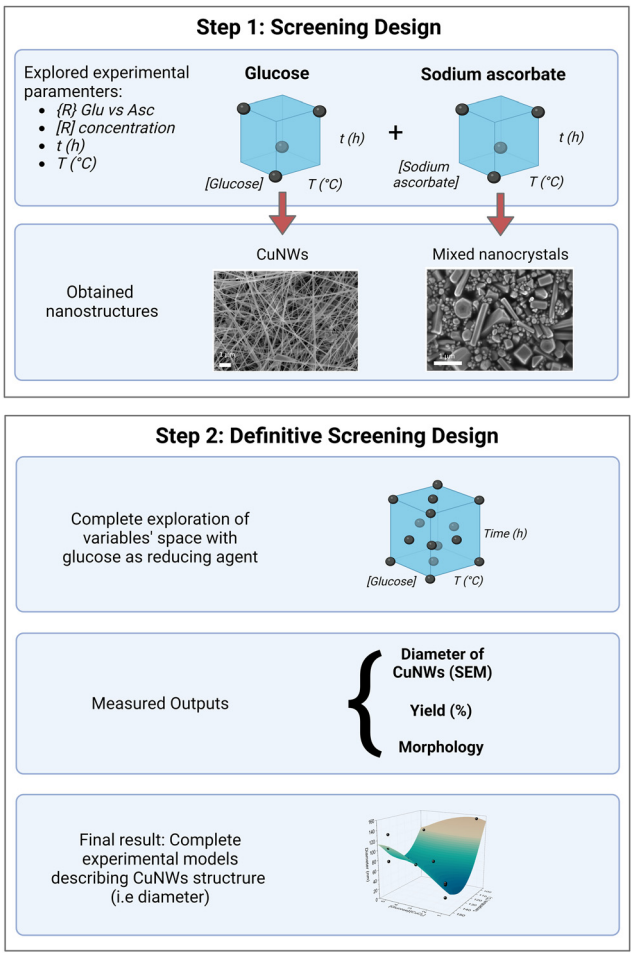

Fig. 1 Workflow to establish the relationship between the synthesis parameters and the morphology of CuNWs, based on a sequential DOE approach.

2.1. Screening design

In the screening phase of the DOE method, we selected four variables known to affect the morphology of the CuNWs, such as the reaction temperature (T), reaction time (t), and type {R} and quantity [R] of reducing agent. These parameters were divided into two levels, resulting in a 2^4 factorial design, comprising a total of 16 experiments: 8 using glucose (A^{glu}–H^{glu}) and 8 using sodium ascorbate as the reducing agent (A^{asc}–H^{asc}). Therefore, there are four parameters, each assuming two levels. The values of the experimental parameters for the two levels are collected in Table 1.

To assess the average size and shapes of the obtained Cu nanostructures, SEM analysis was carried out and the images

Table 1 Parameters (factors) and levels evaluated by DOE

Factor	Symbol	Level (−)	Level (+)
Time (h)	t	3	18
Temperature (°C)	T	100	150
Equivalents of reducing agent (C_R/C_{CuCl_2})	[R]	1	5
Type of reducing agent	{R}	Asc	Glu

collected for each synthesis are presented in Fig. S1 and S2 (ESI†). Under the explored synthesis conditions, the type of reducing agent emerged as the parameter with the most significant impact on the morphology of CuNWs, as evidenced by representative SEM images in Fig. 2 (top row: glucose and bottom row: ascorbate). Glucose synthesis consistently produced long CuNWs with well-defined diameters ranging from 26 to 155 nm and a polydispersity index (PDI) ≤ 0.1. In contrast, sodium ascorbate synthesis yielded mixed structures, including nanoparticles and short, thick CuNWs with an aspect ratio <100 and PDI <0.35.

The screening design highlighted glucose's consistency in producing nanowires with varying diameters and yields (0–66.9%), prompting further exploration to quantify the relationship between synthesis parameters (t, T, and [R]) and morphology *via* the glucose route.

2.2. Definitive screening design

A definitive screening design (DSD) was employed to create a quantitative model linking synthesis parameters to measured outputs, considering linear effects (t, T, and [R]) and second-order effects, which include both quadratic (t^2, T^2, and $[R]^2$) and interaction terms ($t \times T$, $t \times$ [R], and $T \times$ [R]).[50] To include all these additional effects, the DSD expanded on the initial 8 experiments conducted with glucose as the reducing agent, including 10 supplementary experiments at three factor levels according to the experimental design in Table 2, resulting in a total of 18 runs with glucose as the reducing agent. The results are presented in Table 3 that summarizes the average dimensions of the Cu nanostructures for each reaction, the standard deviation, and the PDI. Entries A_{glu}–H_{asc} are related to the preliminary screening phase, while entries I_{glu}–R_{glu} pertain to the definite screening. The DSD generated precise models that effectively described the diameter, aspect ratio, and reaction yield of CuNWs, as detailed in the following paragraphs.

Table 2 Parameters (factors) and levels evaluated in the definitive screening design

Factor	Symbol	Level (−)	Level (o)	Level (+)
Time	T	3	10.5	18
Temperature	T	100	125	150
Equivalents of reducing agent (C_R/C_{CuCl_2})	[R]	1	3	5

2.2.1. Experimental model for the CuNWs' diameter. Multivariate fitting of the experimental diameters yielded a general formula relating the thickness of CuNWs with the experimental parameters, t, T, and [R] (eqn (1)). To generate a simple and easy-to-handle formula, only the factors with a higher statistical significance (p-values ≤ 0.1) were included in the model and in the predictive equations, see Table S1 (ESI†) and related discussion. The resulting diameter describing equation consists of five terms: three terms represent the linear effects of the individual variables ([R], T, and t), one quadratic term for the temperature (T^2), and one term for the interaction between [R] and T. The model demonstrates good linearity, with $R^2 = 0.86$, and a root mean square error (RMSE) of 16.8 nm (Fig. 3A). Fig. 3B and C depict a 3D and a contour plot that graphically represent the relevance of each factor in influencing the measured diameter. The reaction time, which had a lower impact on the thickness of CuNWs (see Table S1, ESI†), was not plotted in 3D plots, but is separately discussed below.

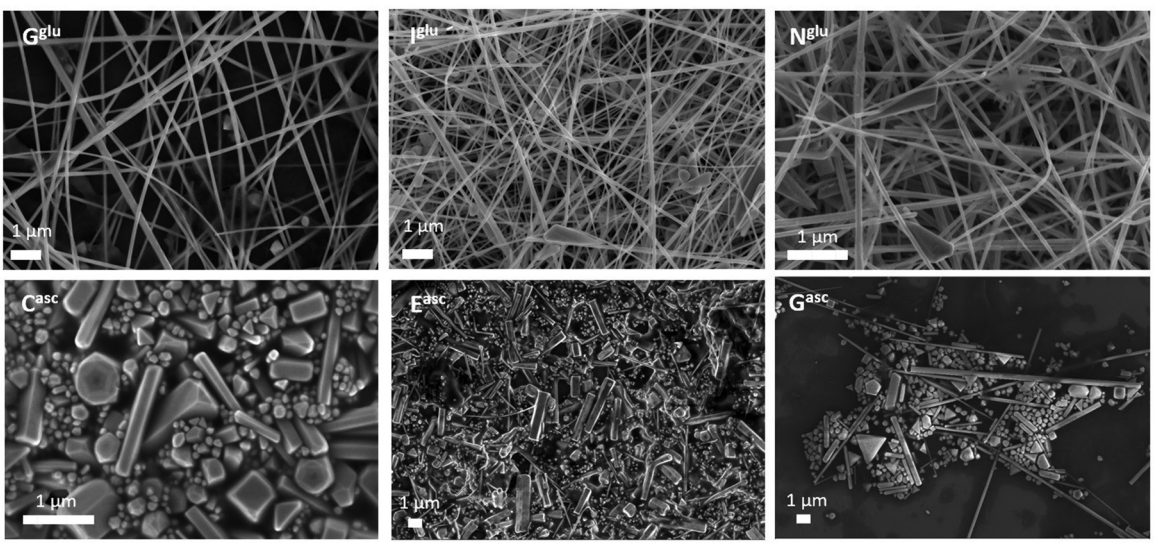

Fig. 2 Representative SEM images from the glucose synthesis route, G^{glu}, I^{glu}, and N^{glu}, and from the sodium ascorbate synthesis route, C^{asc}, E^{asc}, and G^{asc}.

Table 3 Overview of synthesis parameters used, and physicochemical properties obtained for a family of CuNWs obtained

	Experimental factors				Measured outputs								
Entry	{R}	[R]	T (°C)	t (h)	Structure	Yield (%)	d^a (nm)	σ of d^b (nm)	PDI $(\sigma/d)^2$	d of NPs^a (nm)	σ of NPs d^b (nm)	PDI $(\sigma/d)^2$	Ψ
A^{glu}	Glu	1	150	3	NWs	65.7	55	17	0.095	—	—	—	2.73
A^{asc}	Asc	1	100	3	NWs	95.8	215	76	0.125	—	—	—	2.28
B^{asc}	Asc	1	100	3	NWs	96.0	170	58	0.116	—	—	—	2.75
B^{glu}	Glu	1	150	18	NWs	57.1	26	7	0.072	—	—	—	17.21
C^{asc}	Asc	5	150	3	NPs + NRODs	97.4	445	120	0.072	200	66	0.107	2.02
C^{glu}	Glu	3	125	10.5	NWs	50.7	69	21	0.093	—	—	—	17.66
D^{asc}	Asc	1	150	3	NWs	96.2	302	86	0.081	267	48	0.032	2.24
E^{asc}	Asc	5	150	18	NPs + NRODs	88.6	674	230	0.116	406	238	0.344	2.56
D^{glu}	Glu	5	100	3	—	0	—	—	—	—	—	—	—
F^{asc}	Asc	5	150	3	NPs + NRODs	99.3	400	229	0.328	324	92	0.081	1.52
E^{glu}	Glu	1	100	18	NWs	31.9	155	38	0.060	—	—	—	3.15
F^{glu}	Glu	5	100	3	—	0	—	—	—	—	—	—	—
G^{glu}	Glu	5	150	18	NWs	47.5	77	26	0.114	—	—	—	17.67
G^{asc}	Asc	1	100	18	NPs + NWs	99.0	327	192	0.345	466	112	0.058	1.62
H^{glu}	Glu	3	125	10.5	NWs	43.5	62	22	0.126	—	—	—	13.90
H^{asc}	Asc	5	100	18	NPs + NRODs	60.2	559	163	0.085	264	69	0.068	0.44
I^{glu}	Glu	1	100	18	NWs	66.0	115	41	0.127	—	—	—	3.56
J^{glu}	Glu	5	150	3	NWs	49.7	131	29	0.049	—	—	—	7.43
K^{glu}	Glu	1	125	3	—	0	—	—	—	—	—	—	—
L^{glu}	Glu	3	150	18	NWs	56.2	81	18	0.049	—	—	—	15.70
M^{glu}	Glu	3	100	3	—	0	—	—	—	—	—	—	—
N^{glu}	Glu	5	150	3	NWs	41.3	104	17	0.027	—	—	—	3.43
O^{glu}	Glu	5	100	18	NWs	39.1	118	18	0.023	—	—	—	4.15
P^{glu}	Glu	1	150	10.5	NWs	66.9	52	13	0.063	—	—	—	31.30
Q^{glu}	Glu	5	100	10.5	NWs	47.6	101	23	0.052	—	—	—	3.54
R^{glu}	Glu	5	125	18	NWs	59.2	65	16	0.061	—	—	—	22.01

[a] d is the average diameter of CuNWs or CuNRODs estimate by SEM. [b] σ is the standard deviation of d.

Notably, the model displays a curved surface, with a minimum diameter occurring at approximately 140 °C and 1 equivalent of glucose. Within the central flat surface region (135–115 °C and 3–5 eq. of glucose), a saddle point is present, where the diameter remains almost constant.

Moving up from the saddle point, two distinct regions of the experimental surface are noticeable where large diameters are obtained: one at low equivalents of the reducing agent and low temperatures, and the other at high equivalents of the reducing agent and high temperatures. We posit that the curvature of the surface may arise from the coexistence of two mechanisms of Cu(II) reduction mediated by reductones or amines, respectively, both resulting in thick CuNWs. As described by Sue and co-workers, at higher temperature and with a low amount of glucose, the Cu(I)-alkylamine mediated mechanism prevails, whereas at lower temperature and with a higher amount of glucose, the Maillard mediated mechanism does.[49]

The combination of conditions affects mostly the absorption equilibrium of amines on CuNW facets, particularly the (100) and (111) facets which undergo continuous modification during synthesis. Furthermore, the temperature can deeply affect the kinetics of the process.[42] We observed a highly statistically significant interaction between T and [R] (p-value = 0.003, Table S1, ESI†), indicating an interplay between the two variables. Specifically, at a low temperature of 100 °C, the diameter of CuNWs decreased with an increasing glucose concentration, whereas at a high temperature of 150 °C, the diameter increased with the quantity of glucose. These interaction effects have clear implications for optimizing the morphology of CuNWs and are typically only observed and quantified through structured DOE approaches.

$$\text{Diameter [nm]} = 115.56 + 5.60[\text{R}] - 0.42T - 1.39t + 0.43(T - 130.40)([\text{R}] - 3.14) + 0.057(T - 130.40)^2 \quad (1)$$

$$\%\ \text{yield} = -39.21 + 0.57\,T + 1.91t - 0.059(T - 125.00)(t - 10.50) - 0.28(t - 10.50)^2 \quad (2)$$

$$\Psi = -30.85 + 0.39T + 0.34t - 0.038(T - 130.36)(t - 12.64) - 0.30(t - 12.64)^2 - 0.0078(T - 130.35)^2 \quad (3)$$

The reaction time had a minor impact on the thickness of CuNWs, accounting for only 12% of the diameter variation under the explored synthesis conditions (see Table S1, ESI† that lists the percent contribution of each factor to the model). With longer reaction times, the diameter gradually decreased, possibly due to slow corrosion or surface dissolution. Fig. S5 (ESI†) shows the effect of time on the reaction output.

2.2.2. Experimental model for the CuNWs' yield. Thus far, we have analyzed Cu nanocrystal dimensions and shapes. In line with green chemistry principles, it is also crucial to consider the synthesis yield, which has been determined for all reactions and summarized in Table 3. For CuNWs synthesized through the glucose route, the average yield based on the Cu precursor was 42% (on average, the CuNWs were composed of 98.4% in Cu and 1.6% in O from EDX analysis, Table S2 and Fig. S6, S7, ESI†). Multivariate fitting of the yield data was

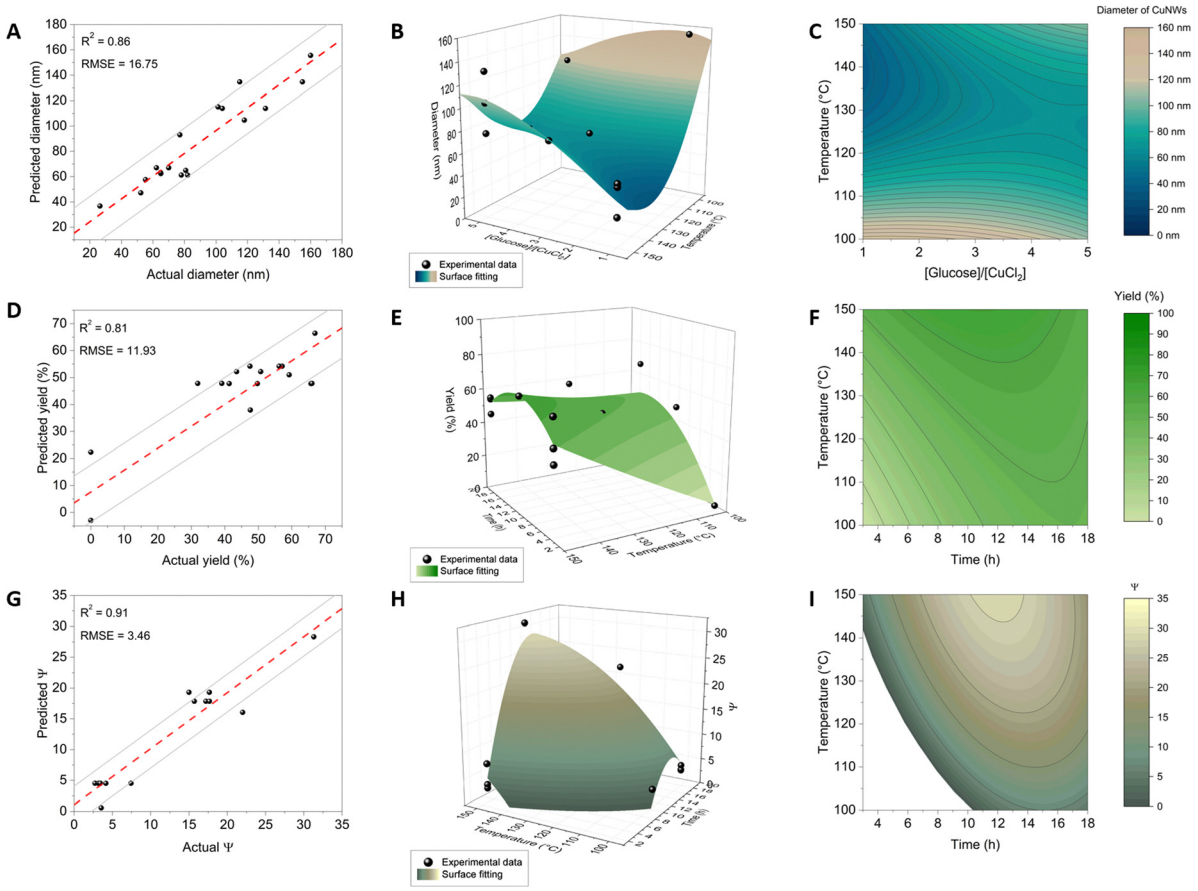

Fig. 3 (A) The prediction model for the CuNW diameter, with the red line representing the linear regression and black dots representing the experimental points. Gray lines are added as visual aids, representing a difference of 20 nm from the linear regression in both positive and negative directions. (B) 3D map of CuNWs diameters correlated with variation in temperature and quantity of glucose. (C) The contour plot of CuNWs' diameter dependence on the temperature and quantity of glucose. (D) The prediction model for the CuNW reaction yield with the red line as the linear regression and black dots as the experimental points. Gray lines are added as a visual aid representing a difference of 10% in yields from the linear regression in both positive and negative directions. (E) The 3D map of the CuNW yield correlated with the variation in the temperature and time. (F) The Contour plot of yield dependence on the temperature and time. (G) The prediction model for Ψ, with the red dotted line representing the linear regression and black dots representing the experimental points. Gray lines are added as visual aids representing a difference of 3 units from the linear regression in both positive and negative directions. (H) The 3D map of Ψ correlated with the variation in the temperature and time. (I) The contour plot of Ψ dependence on the temperature and time.

performed as described above, yielding the prediction expression eqn (2), with a good R^2 value of 0.81 and a RMSE of 11.9 (Fig. 3D). Additionally, Fig. 3E and F show how the yield varies with temperature and time. Interestingly, the yield did not depend on [R], whereas reaction time and temperature, as well as their interaction, considerably affected it. For short reaction times (between 3 h and 12 h), higher temperatures were crucial for achieving a good yield; conversely, at temperatures below 120 °C, the reaction rate dropped substantially. For example, carrying out the reaction at 100 °C for 3 hours did not result in CuNWs formation. This is confirmed, visually, by the aspect of the reaction mixture, as shown if Fig. S8 (ESI†), where it is possible to observe that, in some cases, the product exhibited a light green color, indicating ineffective formation of metallic Cu nanostructures. At 100 °C, the yield increased with time as expected. In contrast, at 150 °C, the yield tends to reach a maximum at around 10 h and then decreasing for longer times. This observation can be explained considering that at 150 °C the kinetics barriers are completely overcome leading to the formation of thermodynamic products in a short time. Our analysis, exemplified by Fig. S5 (ESI†), shows that the evolution of the NW diameter is toward a slight decrease with the reaction time regardless of the temperature and concentration conditions. This evidence supports the hypothesis that a slow corrosion or a surface dissolution process takes place. Interestingly, these processes also affect the reaction yield, which indeed reach an apex along the time-reaction coordinate. On the other hand, operating at 100 °C means that the reduction reaction of Cu proceeds more slowly, and blocking the reaction at a short time does not guarantee the formation of CuNWs. The intermediate temperature conditions are optimal to speed-up the reaction while limiting the side reactions that may occur at higher temperatures.

2.2.3. Experimental model for the CuNW aspect ratio. X-ray diffraction (XRD) analysis served as a pivotal methodological tool for the comprehensive characterization of CuNWs

within the scope of this study, enabling the elucidation of critical compositional and structural attributes, particularly in relation to the synthesis route and aspect ratio of Cu nanostructures. The XRD patterns of the CuNWs obtained in the syntheses A^{glu}–R^{glu} are reported in Fig. S9–S11 (ESI†), revealing, for all samples, diffraction peaks located at $2\theta = 43.34^\circ$, 50.49°, 74.12°, 90.02°, and 95.17°, corresponding to (111), (200), (220), (311), and (222), which are distinctive peaks of Cu.[14,49,51–55] A novel parameter denoted as Ψ, representing the ratio of the magnitudes of (111) and (200) XRD peaks, was introduced to exemplify the aspect ratio. Indeed, previous studies found a correlation between the ratio of the intensity of (111) and (200) peaks and the aspect ratio of CuNWs.[49,56,57] High values of Ψ ($\Psi \gg 1$) indicate CuNWs with high aspect ratio while, on the other side, usually Cu nanocubes show a preferred orientation with (100) planes, displaying a (200) peak with a higher intensity than (111) thus corresponding to $\Psi \ll 1$.[58] Values of Ψ were measured for all CuNWs and are reported in Table 3 and fitted with multivariate analysis to generate the prediction formula in eqn (3). The reaction time and temperature, as well as their interaction, significantly affected Ψ, with an excellent goodness of fit ($R^2 = 0.91$) and a RMSE of 3.46 (Fig. 3G). Fig. 3H and I show the dependence of Ψ on time and temperature, revealing a maximum point at around 140 °C and 12.5 h.

Overall, both the value of Ψ and the reaction yield depended on the same factors (t and T), and their contour plots had similar shapes (in other terms, Ψ and the reaction yield are highly intercorrelated). This can be explained by considering that higher yields promote the growth of longer CuNW crystals, which develop along their long axis. The constancy of the measured diameter values over the reaction time confirms that, after seed formation, the growth of the crystal proceeds in a unique direction. The plots in Fig. 3H and I show that, at any temperature, the NW length increases reaching a maximum after about 12–15 hours, and then decreases with longer reaction times. Since the diameter remains relatively constant, further insight into the effect of the etching process on the wire length has been disclosed. In our opinion, this correlation analysis, rooted in XRD-derived structural insights, furnishes a quantitative framework for tailoring and optimizing synthesis protocols, thereby advancing the precision and efficacy of nanomaterial fabrication processes.

2.2.4. Optimized synthesis conditions for the glucose route. One of the key advantages of DOE-based models is that multiple responses can be optimized simultaneously to target specific applications. As a representative example, let us discuss the case of TCEs used in display technologies, which typically require the production of thin, long CuNWs with a high yield.[58] The best synthesis conditions to obtain such CuNWs can be quickly identified *via* the use of desirability functions within our explored experimental space (refer to the computational details in Fig. S12, ESI†) and are summarized in Table 4. For the TCE example, the optimized conditions include a reaction temperature of 150 °C for 13 h, with 1 equivalent of glucose. These conditions are predicted to produce CuNWs of diameter 43 nm and $\Psi = 28$ in 65% yield. Importantly, these conditions and results are very similar to those of reaction P^{glu} in Table 3, demonstrating the validity of the approach. Within our explored reaction space, optimized reaction conditions for several potential applications of CuNWs are suggested in Table 4.

2.3. Insights into the sodium ascorbate synthesis route

After developing quantitative models for the glucose synthesis route, we present here some insights regarding the syntheses performed employing sodium ascorbate, with which we observed a markedly different pattern in the distribution of nanostructures. Indeed, most of the synthesis yielded Cu nanoparticles (CuNPs) in combination with Cu nanorods, with only the A^{asc}, B^{asc}, and D^{asc} syntheses providing CuNWs as the main products. Under the same conditions, using glucose resulted in CuNWs with a diameter of 55 nm. This effect of the reducing agent emerged from different reduction mechanisms that Cu(II) undergoes when using glucose or sodium ascorbate. Sodium ascorbate is a relatively strong reducing agent. In contrast, glucose is a milder reducing agent. Before becoming active, glucose must react with amines to generate the effective reducing species, the reductone.[6] Syntheses performed employing sodium ascorbate, generally resulted in higher yields (>60%) compared to those using glucose, although with a mixture of morphologies. A further difference to evaluate concerns the nature of the reducing agent in terms of electronic equivalents provided to the metal cation. Ascorbate acts as a bi-electronic reducing agent,[56] meaning that 1 chemical (molar) equivalent of ascorbate counts for 2 electronic equivalents. To understand the role of the reducing agent, we performed a synthesis under the same conditions of F^{asc} (nomenclature refers to Table 2) but employing 0.5 mol eq. of

Table 4 Optimized CuNW synthesis conditions for selected potential applications

Optimized parameters			Optimized conditions			
Diameter[a] (nm)	Ψ[a]	Yield[a] (%)	T (°C)	T (h)	[R] (glucose)	Potential applications
↓(43)	↑(28)	↑(65)	150	13	1	TCEs (displays)
↑(103)	↑(28)	↑(66)	150	11	5	Catalysis (HER, CO_2RR, NO_3RR, and cross-coupling)
↓(43)	Not relevant	↑(66)	150	13	1	Nanoelectronics (thin film transistors and interconnects in integrated circuits)
↑(138)	Not relevant	↑(48)	100	15	1	Energy storage devices (supercapacitors and batteries)

[a] The arrows indicate the desired direction for the parameter (*i.e.*, maximize or minimize), while the value in parenthesis indicates the predicted value for the optimized reaction conditions.

sodium ascorbate. The result of this synthesis is reported in Fig. S13 (ESI†). By using only 0.5 mol eq. of sodium ascorbate, we found that long CuNWs formed (with average diameter equal to 61 nm, yield = 61.3%). There were also some similarities between the two reducing agents. SEM analysis revealed that all the CuNWs exhibited a penta-twinned structure, indicating that the aggregation process of Cu remained consistent across the two reducing agents. This finding agrees with the work of F. Silly *et al.*, which showed that the more stable Cu seed is the penta-twinned one within the temperature range investigated, namely 100–150 °C.[59] For both reducing agents, significant factors such as temperature and concentration of the reducing agent could accelerate the growth of CuNWs and thereby modify their final aspect ratio, Ψ. This parameter was found to be extremely sensitive to the synthesis temperature. Concerning the syntheses carried out employing a high quantity of sodium ascorbate, a common pattern can be observed. Upon inspecting the SEM images in Fig. S2C, E, F, and H (ESI†), it becomes apparent that hollow Cu nanostructures are present. This outcome was achieved when a high concentration (5 eq.) of ascorbate was used. Under these conditions, ascorbate can act as the capping agent and compete with the ODA for the coordination of Cu, thereby significantly affecting the morphology. Moreover, high concentrations of Na^+ ions can also affect the absorption dynamics of the capping agent and thus the growth dynamic of the nanocrystals, resulting in the complete lack of their anisotropic growth. In summary, we have demonstrated that the optimal quantity of sodium ascorbate is crucial for the formation of CuNWs, with 1 eq. or, preferably, 0.5 eq. resulting in the production of thin CuNWs.

2.4. CuNWs-based electrodes preparation, characterization and test in the CO_2RR

Copper-based nanostructures can potentially play a pivotal role in many fields as we highlighted in Table 4 where we correlated the optimized synthetic parameters with the specific range of applications. Among others, here, we describe how our CuNWs spontaneously form a conductive network that we successfully used as electrodes for activating the electrocatalysis of CO_2 reduction. Our approach to employ CuNWs as affective catalysts and electron carriers is illustrated in Fig. 4. We covered an electrochemical inert glass slide with a drop-cast 1 mg mL^{-1}

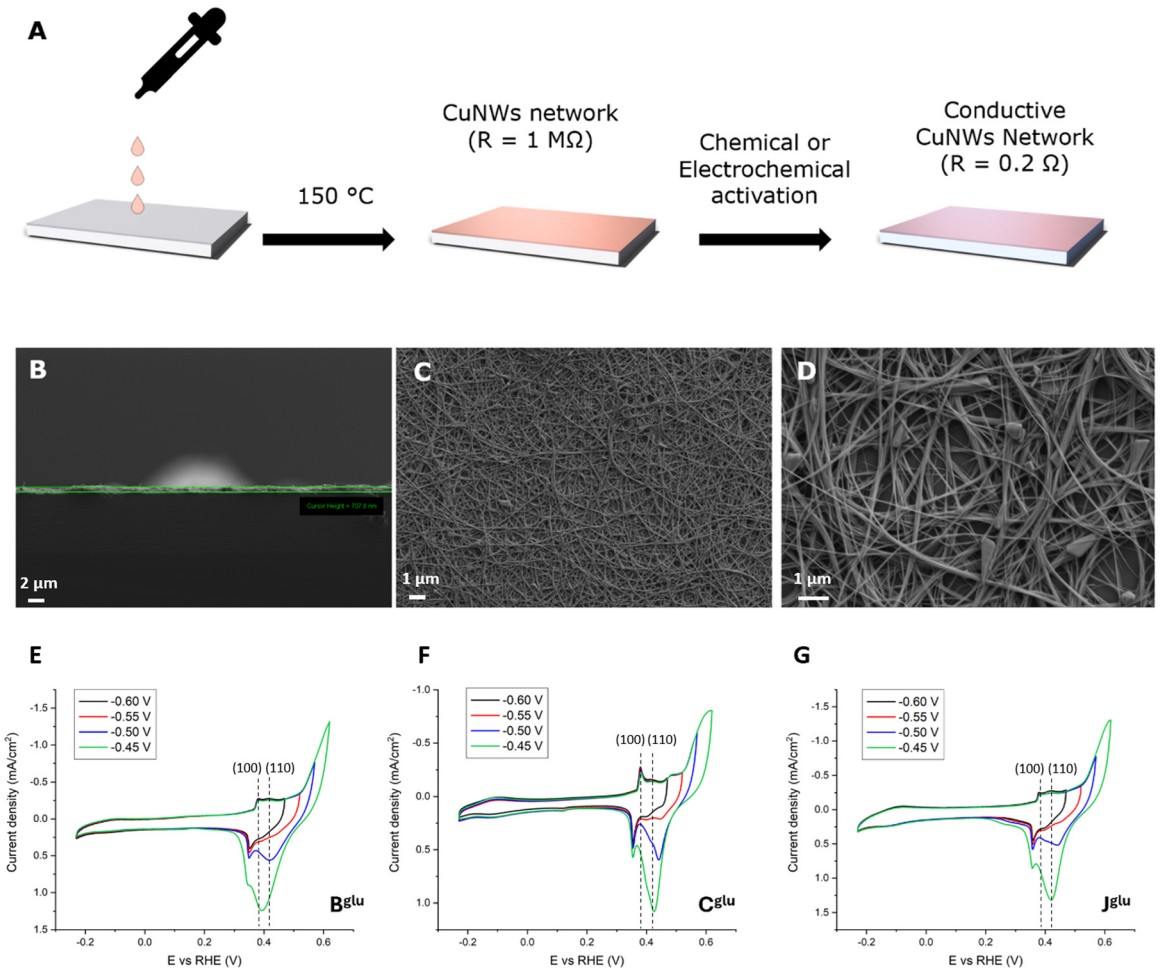

Fig. 4 (A) A scheme of the preparation of CuNW electrodes. (B)–(D) SEM images of the cross-section (B), top view (C), and zoom of the top view (D) of CuNW electrodes. (E) Cyclic voltammetry in 1 M NaOH recorded for B^{glu} (E), C^{glu} (F), and J^{glu} (G) CuNW electrodes. Inverting the potential at different values, the effect of different degrees of Cu(I) oxidation on the voltametric pattern. The vertical dotted lines assign the peaks to crystal facets.

CuNW ethanol solution to obtain an approximately 1 μm thick CuNW film. The evaporation of the solvent and the consequential attachment of the wires to the glass were favored by heating the plate at 150 °C. The drop-casting method yielded CuNW electrodes with an initially high intrinsic resistance, primarily attributed to the native copper oxide layer and to the presence of the capping agent monolayer provided by ODA. Therefore, to establish a percolative charge network among the CuNWs enabling a guaranteed efficient electron transfer, we exploited both chemical and electrochemical treatments by immersing the NWs in a 3 mg mL^{-1} $NaBH_4$ solution for 30 minutes or by applying a constant potential of −1.3 V *versus* RHE for 60 seconds in 1 M $KHCO_3$ solution. From a catalytic point of view, it has been recently pointed out that different copper crystal facets exhibit unique electrocatalytic behaviors within the CO_2 reduction reaction (CO_2RR),[6,60,61] where (111) facets tend to favor methane production, while extended (100) terraces are more selective for ethylene.[62–65] To gain insight into the crystalline structure and defects of the surface of our CuNWs, cyclic voltammetry (CV) characterization studies were carried out in a 1 M NaOH solution to observe the peaks related to the adsorption and desorption of OH^- ions onto the particular crystallographic facets of the CuNWs which serve as fingerprints for each.[65] CV was performed on three NWs selected for their different diameter's sizes: B^{glu} ($\bar{d}$ = 26 nm), C^{glu} ($\bar{d}$ = 69 nm), and J^{glu} ($\bar{d}$ = 131 nm). Fig. 4E–G show the CVs' peaks at +0.37 V and +0.41 V *vs.* RHE that can be attributed to (100) and (110) facets peculiar surface defects, respectively. Additionally, the signal between −0.05 and −0.1 V *vs.* RHE can be assigned to a larger exposed (100) surface. These observations are consistent with previous literature reports.[65–67] Interestingly, the characteristic peak associated with adsorption/desorption on the (111) facet expected at +0.47 V is not clearly detectable in agreement with the small number of exposed boundaries' facets within the wires. Although similar peaks have been observed for the three selected CuNWs, different relative heights can be conferred to each of them with the smaller and larger wires being quite similar, whereas the intermediate exhibits a more pronounced (100) signal. Electrocatalytic investigations were then performed by applying constant potential electrolysis experiments in 1 M $KHCO_3$. Fig. 5A illustrates the relative amount of the detected products other than hydrogen that accounted for the remaining FE not represented. The histograms clearly demonstrate that the three nanowires exhibit different catalytic behaviors. As the diameter increases from B to J, the FE of formate and acetate decreases, indicating reduced selectivity for these products. Conversely, the FE of ethylene follows a distinct pattern: both the smallest (B^{glu}: 26 nm) and the largest (J^{glu}: 131 nm) nanowires produce ethylene with a low FE of approximately 0.5% while the intermediate sample (C^{glu}: 69 nm) shows a 16 times better FE in ethylene formation. This relative superior performance of the C^{glu} CuNWs in terms of efficient electrocatalysts for ethylene production is in agreement with the literature reflecting the presence of the larger response in terms of available (100) active sites compared to the other wires as described above. *Vice versa*,

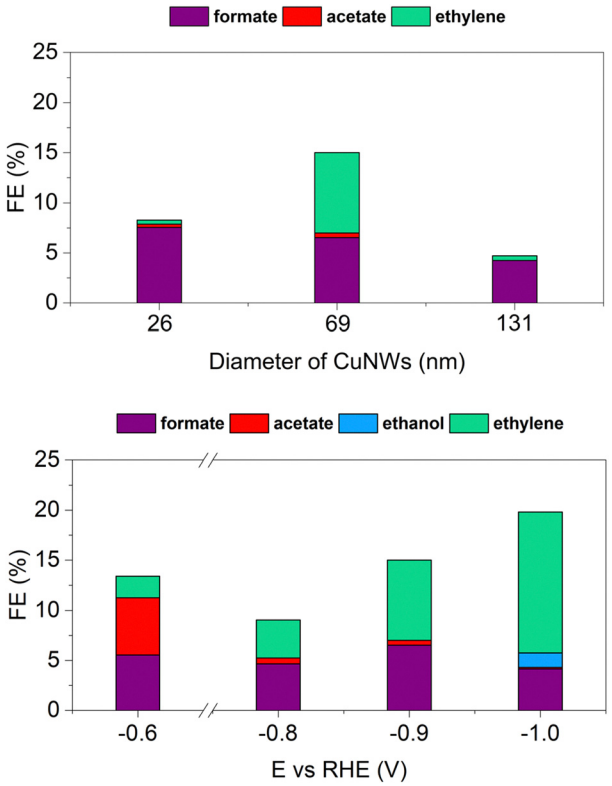

Fig. 5 (A) Faradaic efficiency of three different CuNWs, B^{glu}, C^{glu}, and J^{glu}, at −0.9 V *vs.* RHE in 1 M $KHCO_3$ solution. (B) Faradaic efficiency of C^{glu} at different electrochemical potentials in 1 M $KHCO_3$.

the lower activity of the 26 nm thick B^{glu} wire may also be attributed to mechanical fragility due to their small diameter, resulting in an unstable conductive network during experiments. CuNWs C^{glu} were further tested under varying potentials as described in Fig. 5B. A peculiar trend was detected: while the formate production remains relatively constant across all the tested potentials, the acetate production reaches its maximum at −0.6 V *vs.* RHE with a FE of 5.5%. Ethylene production, on the other hand, nicely increases as the potential becomes more negative, with FE reaching a value of 14% at −1.0 V *vs.* RHE.

3. Experimental

3.1. Reagents

All manipulations were carried out in air using standard laboratory equipment. All the reagents and the solvents were obtained from commercial suppliers and used as received without further purification.

Copper dichloride dihydrated ($CuCl_2{\cdot}2H_2O$, > 99.0% from Merck), 1-octadecyl amine (ODA, from Merck), glucose (>99.5%, from Merck), sodium ascorbate (>98%, from Merck), ethanol (>99.5%, from Merck), isopropanol (>99.8%, from Merck), NaOH (>99% from Merck), and $KHCO_3$ (99.7% from Merck) were used.

3.2. Preparation of CuNWs

The syntheses of CuNWs were performed in a 500 mL flask, closed by a screw cap. A thermostatic oil bath was employed to heat the reaction mixture. Typically, 0.400 g of $CuCl_2{\cdot}2H_2O$ and 2.529 g of 1-octadecylamine (ODA) were added to 200 mL of distilled water. The mixture was mixed and sonicated for 40 minutes at 40 °C. Afterward, x equivalents (x = 1, 3 or 5) of glucose (or sodium ascorbate) with respect to $CuCl_2{\cdot}2H_2O$ were added to the reaction flask, mixed, and heated for x h (x = 3, 10.5 or 18 h) at x °C (x = 100, 125 or 150 °C), without stirring the solution. The reaction conditions and equivalents of reagents employed for the other synthesis are outlined in Table 3. The reaction flask was cooled at room temperature. A red-brownish slurry was formed. Dark red CuNWs precipitated and accumulated in the bottom of the reaction flask. The product was centrifuged at 4000 rpm for 5 minutes using 100 mL of deionized water. This procedure was repeated ten times. Further ten centrifugations were carried out using 50 mL of an absolute ethanol solvent for each wash. The purification process was focused on removing excess reagents and oxidation byproducts of the organic reducing agents, with a minimal loss of copper nanomaterials. The obtained CuNWs were stored at 20 °C in absolute ethanol or isopropanol under an argon-saturated atmosphere. By implementing these storage protocols, we were able to maintain the structural integrity and functionality of the CuNWs over extended periods (6–9 months). To determine the percentage yield, CuNWs were dried, after the purification protocol, employing rotavapor equipment, and weighted accurately. The weight of CuNWs was converted to the percentage yield.

3.3. Materials characterization

3.3.1. X-Ray diffraction. Film XRD measurements were conducted using a Bruker D8 Advance diffractometer, fitted with a LYNXEYE detector in 1D mode (Department of Chemical Sciences, University of Padova). Diffraction data were acquired by exposing powder samples to Cu-Kα1,2 X-ray radiation. X-rays were generated from a Cu anode supplied with 40 kV and a current of 40 mA. The data were collected over the 30–100° 2θ range with a step size of 0.025° 2θ and a nominal time per step of 0.2 s. Fixed divergence slits of 0.50° were used together with Soller slits with an aperture of 2.34°.

3.3.2. Scanning electron microscopy (SEM). SEM was performed with a Zeiss Sigma HD microscope, equipped with a Schottky FEG source, one detector for backscattered electrons and two detectors for secondary electrons (InLens and Everhart Thornley). The microscope is coupled to an EDX detector (from Oxford Instruments, x-act PentaFET Precision) for X-ray microanalysis, working in energy dispersive mode. A low accelerating voltage (2 KV) was used to accurately delineate fine surface features and to avoid conductive coatings that can deleteriously modify surface morphology.

3.3.3. Electrochemical measurements. Cyclic voltammetries were conducted in 1 M NaOH electrolyte solution in a three-electrode set-up, where a CuNWs deposited glass slide acted as a working electrode, a saturated calomel electrode (SCE) as a reference electrode and a Pt wire as a counter electrode. The measurements were carried out in inert atmosphere maintaining an Argon flux in the cell during the experiment.

Electrocatalytic tests were carried out using an H-cell using the CuNW-based electrode as the working and the SCE as the reference electrode in the cathodic chamber. The counter electrode was located on the anodic chamber, and it was constituted using a platinum plate at which the oxygen evolution reaction (OER) occurred. In each compartment, a 50 mL solution of 1 M $KHCO_3$ was present. The electrical communication between the chambers was ensured using a Nafion membrane. The employed potentiostat was a CHI660c workstation (CHInstruments). The liquid and gaseous products obtained from the electrocatalytic experiments were characterized with nuclear magnetic resonance (NMR) and gas chromatography (GC), respectively, and quantified as described in the ESI.† The measurement of the selectivity is expressed in terms of faradaic efficiency, which defines the number of electrons that were consumed to produce a certain product.[21] FE is calculated according to the equation:

$$\mathrm{FE}\% = \frac{znF}{Q} \times 100$$

where z is the number of electrons involved in the process, n is the number of produced moles for a specific product, F is the Faraday constant (96 485 C mol^{-1}) and Q is the total charge consumed during electrolysis. Electrolyses were conducted for 90 minutes.

3.3.4. NMR analysis. The ^{1}H-NMR spectra were acquired with a Bruker Avance 300 NMR spectrometer, working at 23 °C with a 300.1 MHz frequency. The quantitative information was collected by preparing the sample as a mixture of 500 μL of electrolytic solution with the ECO_2RR products, 100 μL of heavy water (D_2O, D 99, 90%, from Eurisotop), and 10 μL of a 7.8 mM dimethyl sulfoxide solution which, indeed, worked as the internal standard. A "pre-saturation of solvent" sequence was adopted in the acquisition method, to suppress the signal of water, which is the most abundant solvent in the sample.

3.3.5. GC analysis. The qualitative and quantitative analyses of the gaseous products of the CO_2RR were performed using an Agilent 8860 gas chromatograph. From the collection bag, 1 mL of the gaseous mixture was withdrawn with a 1 mL Hamilton syringe and injected into the instrument. Two detectors were employed for different products: a flame ionization detector (FID) for hydrocarbons and a thermal conductivity detector (TCD) for other gases, such as H_2, O_2, and N_2. The separation of the products was achieved using two columns: HO Plot U 19095P-UO4 (30 m × 0.53 mm × 20 μm: length × internal diameter × internal film's thickness) and HP Plot 19095P-MS0 (30 m × 0.53 mm × 50 μm). The eluent phases used were argon or helium.

4. Conclusions

We demonstrated that a multiparametric DOE approach can be effectively exploited to foresee the reaction yield and the

morphological properties of CuNWs, enabling a sound control over their hydrothermal synthesis. For the first time, to our knowledge, the effects of four straightforward synthetic parameters such as the temperature, reaction time, and type and quantity of reducing agents were elucidated by establishing a correlation between the CuNWs' dimensions and physicochemical properties.

Notably, our methodology allows the production of nanostructures with a wide range of diameters and aspect ratios without severe modification of the synthetic setup. As proved by SEM and XRD analyses, the use of sodium ascorbate as the reducing agent induces the formation of thicker and shorter CuNWs compared to those produced with glucose, while an extended reaction time allows longer CuNWs to be synthesized up to hundred microns. In this scenario, our DOE procedure guarantees the CuNWs' morphological control over a virtual infinitive possibility, thus offering a roadmap for leveraging Cu based materials as robust nanostructures suitable for further surface chemical and physical engineering. The employed hydrothermal method has already been upscaled with success[68] and along with the manageable temperature range employed and the use of inexpensive and environmentally friendly reagents, the overall process appears promising for industrial developments. Beyond these successful synthetic results based on the DOE approach, we also drove our Cu-based nanostructures towards industrial developments exploiting their functionality as electrocatalysts. We not only highlighted that CuNWs are easy-to-operate electrodes forming a highly conductive network able to effectively work on inert supports but also that they can be further improved as electrocatalysts for CO_2 reduction. The intrinsic permeability and flexibility of CuNWs make them well-suited as gas diffusion electrodes in flow setups enabling the overcoming of the slow diffusion kinetics of reagents and increasing catalyst efficiency, thus paving the way for the realization of environmentally conscious and resource-efficient technologies.

Data availability

The data supporting the findings of this study are available within the article main text and the ESI† in the form of tables, figures, images and equations.

Conflicts of interest

There are no conflicts to declare.

Acknowledgements

The authors are grateful to the financial support from the European Research Council (ERC) under the European Union's Horizon 2020 research and innovation program (grant agreement no. 949087) (A. A.), the Department of Chemical Sciences of the University of Padova [P-DiSC#01BIRD2019-UNIPD] (M. B.), the University of Padova – Supporting Talent in Research – STARS 2019 "TimeForResponse" grant 166081 (S. B.), and the Basell Poliolefine Italia S.r.l. (A. C.). The authors thank Dr Andrea Basagni (University of Padova) for technical support in taking SEM images and profitable discussion on XRD data.

Notes and references

1 L. Cademartini, G. A. Ozin and J. M. Lehn, *Concept of Nanochemistry*, Wiley, 2009.
2 Z. Lyu, Y. Shang and Y. Xia, *Acc. Mater. Res.*, 2022, **3**, 1137–1148.
3 C. Choi, J. Cai, C. Lee, H. M. Lee, M. Xu and Y. Huang, *Nano Res.*, 2021, **14**, 3497–3501.
4 O. Baranov, K. Bazaka, T. Belmonte, C. Riccardi, H. E. Roman, M. Mohandas, S. Xu, U. Cvelbar and I. Levchenko, *Nanoscale Horiz.*, 2023, **8**, 568–602.
5 M. S. Xie, B. Y. Xia, Y. Li, Y. Yan, Y. Yang, Q. Sun, S. H. Chan, A. Fisher and X. Wang, *Energy Environ. Sci.*, 2016, **9**, 1687–1695.
6 A. Conte, M. Baron, S. Bonacchi, S. Antonello and A. Aliprandi, *Nanoscale*, 2023, **15**, 3693–3703.
7 K. Rossi and R. Buonsanti, *Acc. Chem. Res.*, 2022, **55**, 629–637.
8 J. Zhang, W. Luo and A. Zuttel, *J. Mater. Chem. A*, 2019, **7**, 26285–26292.
9 M. Strach, V. Mantella, J. R. Pankhurst, P. Iyengar, A. Loiudice, S. Das, C. Corminboeuf, W. V. Beek and R. Buonsanti, *J. Am. Chem. Soc.*, 2019, **141**, 16312–16322.
10 G. Zhang, Z.-J. Zhao, D. Cheng, H. Li, J. Yu, Q. Wang, H. Gao, J. Guo, H. Wang, G. A. Ozin, T. Wang and J. Gong, *Nat. Commun.*, 2021, **12**, 5745.
11 Z. Han, D. Han, Z. Chen, J. Gao, G. Jiang, X. Wang, S. Lyu, Y. Guo, C. Geng, L. Yin, Z. Wenig and Q.-H. Yang, *Nat. Commun.*, 2022, **13**, 3158.
12 H. Guo, N. Lin, Y. Chen, Z. Wang, Q. Xie, T. Zheng, N. Gao, S. Li, J. Kang, D. Cai and D. L. Peng, *Sci. Rep.*, 2013, **3**, 2323.
13 J. Gao, A. Bahmanpour, O. Kröcher, S. M. Zakeeruddin, D. Ren and M. Grätzel, *Nat. Chem.*, 2023, **15**, 705–713.
14 Y. Zhang, Z. Si, H. Du, Y. Deng, Q. Zhang, Z. Wang, Q. Yu and H. Xu, *Inorg. Chem.*, 2022, **61**, 20666–20673.
15 K. Shi, M. D. Willis, Z. Ren and X. Feng, *J. Phys. Chem. C*, 2023, **127**, 20710–20717.
16 S. R. Waldvogel, S. Lips, M. Selt, B. Riehl and C. J. Kampf, *Chem. Rev.*, 2018, **118**, 6706–6765.
17 H. Guo, N. Lin, Y. Chen, Z. Wang, Q. Xie, T. Zheng, N. Gao, S. Li, J. Kang, D. Cai and D. L. Peng, *Sci. Rep.*, 2013, **3**, 2323.
18 O. Ohiienko and Y. J. Oh, *Mater. Chem. Phys.*, 2020, **246**, 122783.
19 T. H. Duong and H. C. Kim, *Ind. Eng. Chem. Res.*, 2018, **57**, 3076–3082.
20 Y. Zhao, L. Fan, Y. Zhang, H. Zhao, X. Li, Y. Li, L. Wen, Z. Yan and Z. Huo, *ACS Appl. Mater. Interfaces*, 2015, **7**, 16802–16812.
21 Q. Li, S. Fu, X. Wang, L. Wang, X. Liu, Y. Gao, Q. Li and W. Wang, *ACS Appl. Mater. Interfaces*, 2022, **14**, 57471–57480.

22 C. Choi, S. Kwon, T. Cheng, M. Xu, P. Tieu, C. Lee, J. Cai, H. M. Lee, X. Pan, X. Duan, W. A. Goddard and Y. Huang, *Nat. Catal.*, 2020, **3**, 804–812.
23 S. Zhao, F. Han, J. Li, X. Meng, W. Huang, D. Cao, G. Zhang, R. Sun and C.-P. Wong, *Small*, 2018, **14**, 1800047.
24 J. C. Yu, F. G. Zhao, W. Shao, C. W. Geb and W. S. Li, *Nanoscale*, 2015, **7**, 8811–8818.
25 M. Mohl, P. Pusztai, A. Kukovecz and Z. Konya, *Langmuir*, 2010, **26**, 16496–16502.
26 C. Kim, W. Gu, M. Briceno, I. M. Robertson, H. Choi and K. Kim, *Adv. Mater.*, 2008, **20**, 1858–1863.
27 N. Ulrich, M. Schäfer, M. Römer, S. D. Straub, S. Zhang, J. Brötz, C. Trautmann, C. Scheu, B. J. M. Etzold and M. E. T. Molares, *ACS Appl. Nano Mater.*, 2023, **6**, 4190–4200.
28 Z. Liu, Y. Yang, J. Liang, Z. Hu, S. Li, S. Peng and Y. Qian, *J. Phys. Chem. B*, 2003, **107**, 12658–12661.
29 S. Li, Y. Chen, L. Huang and D. Pan, *Inorg. Chem.*, 2014, **53**, 4440–4444.
30 M. Kevin, G. Y. R. Lim and G. W. Ho, *Green Chem.*, 2015, **17**, 1120–1126.
31 S. Bhanushali, P. Ghosh, A. Ganesh and W. Cheng, *Small*, 2015, **11**, 1232–1252.
32 Z. Tang, H. Kwon, M. Yi, K. Kim, J. W. Han, W. S. Kim and T. Yu, *ChemistrySelect*, 2017, **2**, 4655–4661.
33 C. Hwang, J. An, B. Doo Choi, K. Kim, S.-W. Jung, K. J. Baeg, M.-G. Kim, K. M. Ok and J. Hong, *J. Mater. Chem. C*, 2016, **4**, 1441–1447.
34 S. Xu, X. Sun, H. Ye, T. You, X. Song and S. Sun, *Mater. Chem. Phys.*, 2010, **120**, 1–5.
35 J. Chen, F. Jiang and Y. Yin, *Acc. Chem. Res.*, 2021, **54**(5), 1168–1177.
36 R. Leardi, *Anal. Chim. Acta*, 2009, **652**, 161–172.
37 E. M. Williamson, Z. Sun, L. M.-Tamez and R. L. Brutchey, *Chem. Mater.*, 2022, **34**, 9823–9835.
38 R. S. Fernandes, I. M. Raimundo and M. F. Pimentel, *Colloids Surf., A*, 2019, **577**, 1–7.
39 E. M. Williamson, B. A. Tappan, L. Mora-Tamez, G. Barim and R. L. Brutchey, *ACS Nano*, 2021, **15**, 9422–9433.
40 T. Pretto, F. Baum, G. F. S. Andradeb and M. J. L. Santos, *CrystEngComm*, 2021, **23**, 397–403.
41 F. Baum, T. Pretto, R. A. Gouvea and M. J. L. Santos, *Cryst. Growth Des.*, 2022, **22**, 3669–3679.
42 J. C. de la Rosa and M. Segarra, *ACS Omega*, 2019, **4**, 18289–18298.
43 E. M. Williamson and R. L. Brutchey, *Inorg. Chem.*, 2023, **62**, 16251–16262.
44 H. Tao, T. Wu, M. Aldeghi, T. C. Wu, A. A. Guzik and E. Kumacheva, *Nat. Rev. Mater.*, 2021, **6**, 701–716.
45 E. J. Braham, R. D. Davidson, M. Al-Hashimi, R. Arroyave and S. Banerjee, *Dalton Trans.*, 2020, **49**, 11480–11488.
46 H. J. Yang, S. Y. He and H. Y. Tuan, *Langmuir*, 2014, **30**, 602–610.
47 T. Zhang, W. Y. Hsieh, F. Daneshvar, C. Liu, S. P. Rwei and H. J. Sue, *Nanoscale*, 2020, **12**, 17437–17449.
48 J. Cure, A. Glaria, V. Collière, P. F. Fazzini, A. Mlayah, B. Chaudret and P. Fau, *J. Phys. Chem. C*, 2017, **121**, 5253–5260.
49 H. Yoon, D. S. Shin, B. Babu, T. G. Kim, K. M. Song and J. Park, *Mater. Des.*, 2017, **132**, 66–71.
50 B. J. Jones and C. Nachtsheim, *J. Qual. Technol.*, 2011, **43**, 1–15.
51 Y. Zheng, J. Liang, Y. Chen and Z. Liu, *RSC Adv.*, 2014, **4**, 41683–41689.
52 H. Guo, N. Lin, Y. Chen, Z. Wang, Q. Xie, T. Zheng, N. Gao, S. Li, J. Kang, D. Cai and D. L. Peng, *Sci. Rep.*, 2013, **3**, 2323.
53 D. V. R. Kumar, A. M. Koshy, N. Sharma, N. Thomas and P. Swaminathan, *ACS Omega*, 2023, **8**, 21107–21112.
54 Y. Zhang, Z. Si, H. Du, Y. Deng, Q. Zhang, Z. Wang, Q. Yu and H. Xu, *Inorg. Chem.*, 2022, **61**, 20666–20673.
55 C. S. Lewis, L. Wang, H. Liu, J. Han and S. S. Wong, *Cryst. Growth Des.*, 2014, **14**, 3825–3838.
56 J. Y. Lin, Y.-L. Hsueh and J. J. Huang, *J. Solid State Chem.*, 2014, **214**, 2–6.
57 D. V. R. Kumar, I. Kim, Z. Zhong, K. Kim, D. Lee and J. Moon, *Phys. Chem. Chem. Phys.*, 2014, **16**, 22107–22115.
58 Y. Tu, D. Njus and H. B. Schlege, *Org. Biomol. Chem.*, 2017, **15**, 4417–4431.
59 F. Silly and M. R. Castell, *ACS Nano*, 2009, **3**, 901–906.
60 J. M. Chiu, I. Wahdini, Y. N. Shen, C. Y. Tseng, J. Sharma and Y. Tai, *ACS Appl. Energy Mater.*, 2023, **6**, 5058–5066.
61 S. Jeong, C. Huang, Z. Levell, R. X. Skalla, W. Hong, N. J. Escorcia, Y. Losovyj, B. Zhu, A. N. B. Griffith, Y. Liu, C. W. Li, D. R. Hickey, Y. Liu and X. Ye, *J. Am. Chem. Soc.*, 2024, **146**(7), 4508–4520.
62 Y. Hori, I. Takahashi, O. Koga and N. Hoshi, *J. Mol. Catal. A: Chem.*, 2003, **199**, 39–47.
63 Y. C. Zhang, X. L. Zhang, Z. Z. Wu, Z. Z. Niu, L. P. Chi, F. Y. Gao, P. P. Yang, Y. H. Wang, P. C. Yu, J. W. Duanmu, S. P. Sun and M. R. Gao, *Proc. Natl. Acad. Sci. U. S. A.*, 2024, **121**, e2400546121.
64 G. Zhang, Z. J. Zhao, D. Cheng, H. Li, J. Yu, Q. Wang, H. Gao, J. Guo, H. Wang, G. A. Ozin, T. Wang and J. Gong, *Nat. Commun.*, 2021, **12**, 5745.
65 A. K. Engstfeld, T. Maagaard, S. Horch, I. Chorkendorff and I. E. L. Stephens, *Chem. – Eur. J.*, 2018, **24**, 17743–17755.
66 A. Tiwari, H. H. Heenen, A. S. Bjørnlund, T. Maagaard, E. Cho, I. Chorkendorff, H. H. Kristoffersen, K. Chan and S. Horch, *J. Phys. Chem. Lett.*, 2020, **11**, 1450–1455.
67 S. Liu, Y. Li, D. Wang, S. Xi, H. Xu, Y. Wang, X. Li, W. Zang, W. Liu, M. Su, K. Yan, A. C. Nielander, A. B. Wong, J. Lu, T. F. Jaramillo, L. Wang, P. Canepa and Q. He, *Nat. Commun.*, 2024, **15**, 5080.
68 Q. Q. Fu, Y. D. Li, H. H. Li, L. Xu, Z. H. Wang and S. H. Yu, *Langmuir*, 2019, **35**, 4364–4369.